RSC Advances

PAPER

View Article Online
View Journal | View Issue

Cite this: *RSC Adv.*, 2017, **7**, 559

Nano-hydroxyapatite reinforced polyphenylene sulfide biocomposite with superior cytocompatibility and *in vivo* osteogenesis as a novel orthopedic implant†

Yi Deng,[a] Yuanyi Yang,[d] Yuan Ma,[c] Kexia Fan,[c] Weizhong Yang*[b] and Guangfu Yin[b]

The design of novel functional biomaterials that possess similar mechanical attributes as human bones, accompanied with admirable osteogenesis to replace conventional metallic implants would be an intriguing accomplishment, especially in the orthopedic, craniomaxillofacial and dental fields where biointerfaces with outstanding osseointegration are in high demand. Guided by this purpose, in the current study, nano-hydroxyapatite reinforced polyphenylene sulfide (PPS/nano-HA) biocomposites *via* a process of compounding and injection-molding, in an attempt to elevate the bioactivity and osteogenic properties of PPS, were successfully developed for the first time. The resultant binary composites were characterized in terms of topological structure, chemical composition, hydrophilicity, and water uptake capacity. Mechanical property evaluation revealed that the elastic modulus of the PSS/nano-HA composites was closer to that of natural bones. Besides, *in vitro* cytotoxicity, cell proliferation, alkaline phosphatase activity, osteocalcin expression and calcium mineral deposition all disclosed that the PSS/nano-HA bioactive composites evoked better cell viability and osteo-differentiation of osteoblasts on account of the contribution of the doped nano-HA. To our delight, *in vivo* assessment of the calvarial defect model by means of soft X-ray, histological observation, and real-time PCR analysis after 8 weeks confirmed the dramatically accelerated osteogenesis and osteointegration. Overall, our findings demonstrated that the nano-HA enriched PPS biocomposites with impressive cytocompatibility and osteogenic functions hold large potential in load-bearing orthopedic and dental applications. In addition, this work will, as expected, offer a crucial scientific basis and experimental fundamentals to support the adoption of PPS-based biomaterials as new hard tissue repair materials for further clinical therapy.

Received 20th October 2016
Accepted 14th November 2016

DOI: 10.1039/c6ra25526d

www.rsc.org/advances

1. Introduction

Bone defects resulting from disease, aging, trauma, congenital abnormalities and surgical resections remain a serious fast-growing challenge in the medical area worldwide, and the associated annual healthcare expenditures are estimated to be tens of billions of dollars with a prominent increase over the coming decades.[1,2] When irreparable bone damage occurs, and it cannot be regenerated by the in-house self-healing process of human body, orthopedic and dental implants are much-needed in clinic. Currently, the popular orthopedic biomaterials are still traditional metals such as titanium (Ti) alloys, stainless steels, cobalt-based alloys and so on, because of their unique characteristics in chemical constitution, mechanics, and biocompatibility.[3,4] There are concerns, nevertheless, regarding potential release of harmful metal ions and radiopacity of metal alloys *in vivo*. Moreover, the mismatched elasticity between adjacent bone tissues and metals leads to implant failure and even bone resorption.[5,6] To overcome these limitations, the design of innovative synthetic polymer with the goal of subrogating for metals is extensively pursued, and encourages an emerging area in the fields of orthopaedics, dentistry, and neurosurgery over the recent years.

Some high-performance engineering plastics (HPEPs) including polyetheretherketone (PEEK),[7–10] and polyphenylene sulfide (PPS), have a tremendous potential to replace metallic implants worthy of serious consideration for the following reasons: (1) different from metallic materials which present a large elastic modulus of over 100 GPa, whereas the two HPEPs

[a]School of Chemical Engineering, Sichuan University, Chengdu 610065, China
[b]College of Materials Science and Engineering, Sichuan University, Chengdu 610065, China. E-mail: scuywz@139.com
[c]Department of Neurosurgery, Chengdu Military General Hospital, Chengdu 610083, China
[d]Department of Materials Engineering, Sichuan College of Architectural Technology, Deyang 618000, China

† Electronic supplementary information (ESI) available. See DOI: 10.1039/c6ra25526d

has an elastic moduli between 2–4 GPa (PEEK ≈ 3–4 GPa;[5,11] PPS ≈ 2–4 GPa (ref. 12 and 13)) closer to that of human cortical bone (about 18 GPa), which can mitigate concerns over the potential metal ion release and the risks of osteanabrosis and bone resorption caused by stress shielding.[14] (2) The outstanding chemical resistance of PEEK and PPS can avoid the degradation caused by bio-corrosion, which often occurs on metallic implants. (3) PEEK and PPS, non-resorbable thermoplastic polymer, displayed the natural radiolucency, even magnetic resonance imaging (MRI) compatibility, and bioinertness nature, eliciting no positive response in the body.[15] In the orthopaedic clinic, PEEK implants has been fabricated into spine cages for vertebral fusion, patient specific craniomaxillofacial implants such as skull plates and as arthroscopic suture anchors to repair anterior cruciate ligaments,[16,17] since receiving USA Food and Drug Administration (FDA) approval in the late 1980s, but there is no publication focusing on PPS as potential biomaterials used in biomedical fields and medical devices.

PPS, a semi-crystalline polymer, that possesses an approximate crystallinity (X_c) of 29–36%, glass transition temperature (T_g) of about 85 °C, and melting point (T_m) at ~272 °C,[18] has harvested a considerable interest for numerous challenging applications ranging from aerospace science to industrial use.[19,20] From the processing perspective, it is more readily manufactured by conventional plastic processing equipments, and shaped by machining and heat contouring to fit the shape of bones due to lower melting point and processing temperature compared with PEEK (melting point = 334 °C). In addition to abundant yield, lower production cost and comparative mechanical characteristics to PEEK can make PPS become a more potent candidate as bone-grafting materials than PEEK. However, some drawbacks such as bioinertness and inferior osteoconduction of PPS likewise impede its further application in clinic. Combining polymers with bioactive inorganic materials, such as β-tricalcium phosphate (β-TCP),[21,22] hydroxyapatite (HA)[23,24] and titanium dioxide (TiO_2)[25,26] through blending is considered a fascinating and advisable strategy to built biocomposite with appropriate properties for orthopedic purposes, because native bone *per se* is an organic–inorganic biocomposite organized on micro- and nanoscale.[27]

In view of the immanent osteoconduction and osseointegration potence,[28] nano-hydroxyapatite (nano-HA, $Ca_{10}(PO_4)_6(OH)_2$), the chief mineral component of bone matrix, is one of the most appealing inorganic materials for applications in bone regenerative medicine, and therefore has been widely employed in hard tissue engineering to promote biological properties of bioinert polymer *via* compound approach.[29,30] For instance, Yubao Li and his group previously constructed polyamide 66/nano-HA (PA66/nano-HA) composites by incorporating nano-HA particles within PA66 matrix to improve its stiffness, biocompatibility, and osteogenic differentiation activity.[31,32] A PEEK/nano-HA biocomposite through twin screw extruder and injection molding was lately prepared in our lab as dental implant material. Compared to pure PEEK, the composite containing nano-HA exhibited enhanced mechanical behaviors, and favorable adhesion, proliferation and osteogenic conversion of human mesenchymal stem cells (hMSCs), as well as superior *in vivo* osseointegration in canine alveolar bone.[5] Despite the attractive merits and progress in development of various high-performance biocomposites, the employment of HA as nano-reinforcement in PPS-based composites bestowing osteogenic activity and osseointegration on PPS for load-bearing orthopedic applications, to the best of our current knowledge, has not yet been investigated and reported. Herein, the aims of the present work are (1) to develop and characterize the foregoing PPS/nano-HA binary composite; (2) to investigate *in vitro* how osteoblast-like MG-63 cells responded on the nano-HA doped PPS interfaces in terms of proliferation, alkaline phosphatase (ALP) activity, osteocalcin (OCN) secretion, and extracellular matrix (ECM) mineralization; (3) to assess *in vivo* osteogenesis ability of bony tissue exposed to the biocomposite in rat calvarial defect model. This study is intended to help broaden the clinic application and expedite the pace of PPS-based materials to orthopedic/dental implants.

2. Materials and methods

2.1. Materials

Calcium nitrate tetrahydrate ($Ca(NO_3)_2\cdot 4H_2O$), ammonium phosphate dibasic ($(NH_4)_2HPO_4$), tetramethylene sulfone ($C_4H_8O_2S$), dimethylsilicone oil ($(C_2H_6OSi)_n$, $\rho = 0.963$ g cm^{-3}), and absolute ethyl alcohol (C_2H_5OH) were provided by Chengdu Kelong Reagent Co., Ltd. (China). Ammonium hydroxide ($NH_3\cdot H_2O$, 25–28%) was purchased from Chongqing Maoye Reagent Co., Ltd. (China). Polyphenylene sulfide (PPS, $(-C_6H_4\text{-}4\text{-}S-)_n$, $M_n \approx 10\,000$ g mol^{-1}) powders with the density of about 1.34 g cm^{-3} were supplied from Sichuan Deyang Chemical Co., Ltd. (China). (3-Aminopropyl)triethoxysilane (APTES, $H_2N(CH_2)_3Si(OC_2H_5)_3$) was obtained from Sichuan Huatong Co., Ltd. (China). All other chemicals were of analytical reagent grade and were used as received unless noted. All aqueous solutions were prepared with de-ionized water (D.I. water).

2.2. Synthesis of nano-HA particles

Nano-HA was synthesized in our laboratory *via* chemical precipitation method: firstly, $Ca(NO_3)_2$ and $(NH_4)_2HPO_4$ were dissolved in D.I. water separately according to a Ca/P molar ratio of 1.67/1. Then, $(NH_4)_2HPO_4$ solution was slowly dropped into $Ca(NO_3)_2$ solution with continuous stirring. Apatite growth occurred when kept at 40 °C for 6 h in an oil-bath, and the pH value of supernatant was adjusted and maintained to approximate 10 by addition of $NH_3\cdot H_2O$ during the whole experiment. The reaction of HA can be expressed by the reaction:

$$10Ca^{2+} + 6HPO_4^{2-} + 8OH^- \rightarrow Ca_{10}(PO_4)_6(OH)_2 + 6H_2O \quad (1)$$

After reaction, HA slurry was aged for 24 h at room temperature, and the precipitate was obtained after washing with D.I. water and ethanol at least three times, respectively. Finally, the prepared nano-HA particles was air-dried overnight in an oven at 80 °C for future use and characterization.

2.3. Preparation of PPS/nano-HA biocomposites

PPS/nano-HA binary composite containing 30 wt% and 40 wt% nano-HA powders were fabricated by two different approaches: (1) solid–solid blending (physical blending) of PPS and nano-HA: in briefly, a defined amount of PPS, nano-HA powders, and APTES (1 wt%) were blended in a QM-3B high-speed vibrating ball mill (Nanjing T-Bota Scietech Instruments & Equipment Co., Ltd., China) at a mixing speed of 500 rpm for 1 h. APTES was used as coupling agent to increase the dispersity and bonding strength of nano-HA and PPS in the present study. Following this, the resulting mixtures were then dried at 80 °C for 12 h. (2) Liquid–liquid compounding of PPS and nano-HA: the PPS powder was first dissolved in tetramethylene sulfone at a concentration of 20 w/v%, and the obtained nano-HA was re-suspended in D.I. water by ultrasonic and vigorous stirring to yield a nano-HA slurry. Then, PPS solution, nano-HA slurry and 1 wt% APTES were put into a three-necked bottle and compounded at 120 °C in an oil-bath under nitrogen (N_2) atmosphere for 4 h to remove the water. The use of N_2 was to prevent the oxidation of PPS. After complete dehydration, the temperature of sample was elevated to 174 °C for 5 h. The PSS/nano-HA mixture was rinsed with hot D.I. water and ethanol at least three times respectively, and dried at 80 °C for 12 h.

Finally, these PPS/nano-HA binary composites prepared from solid–solid blending and liquid–liquid compounding methods were all producted with a CJ-150M2 injection-molding machine (Zhengxiong Injection Molding Machine Co., Ltd., Shenzhen, China) at an injecting and molding temperature of 300 °C under a load of 30 MPa. After reaching the target temperature, the temperature and pressure were held for 10 min. Then the die and samples were air cooled to 150 °C, and the samples were removed from the molds. All samples were cut into 2 mm thick disks with diameter of 10 mm for surface characterization and *in vitro* testing, and 1 mm thick disks with diameter of 6 mm for *in vivo* measurement. Bare PPS samples were also prepared in the light of the same process and cut into the same shapes as control group. The specific synthetic condition of each sample was listed in Table 1.

2.4. Morphological and physic-chemical characterization

The crystalline phase of as-prepared nano-HA was examined by X-ray diffraction (XRD, XpertTRO MPD, Philips, Netherlands) using a Cu target as radiation source ($\lambda = 1.540598$ Å) at 40 kV. The diffraction angles (2θ) were set between 10° and 70°, with an incremental step size of 4° min^{-1}. The phase identification was achieved by comparing the sample diffraction pattern with standard cards in ICDD-JCPDS database.

The microstructure of nano-HA crystals was carried out using transmission electron microscopy (TEM, Tecnai G2 F20, FEI, USA) with an operating voltage of 100 kV. Samples for TEM imaging were dispersed into ethanol by ultrasonic waves, and the suspension was dropped onto carbon-coated copper grids, air-dried before observation.

Nitrogen adsorption–desorption isotherms of samples were collected on micromeritics porosimeter (Tristar 3000, Micrometrics Instrument Corp., USA) at 77 K under a continuous adsorption condition.

Fourier transform infrared (FT-IR, Magna-IR 750, Nicolet, USA) spectra was collected to identify the functional groups of the HA powders, PPS and PPS/nano-HA composites in the range of 400–4000 cm^{-1}.

The surface hydrophilicity was determined by a contact angle goniometry (JC200C1, Shanghai Zhongchen Digital Technic Apparatus Co., Ltd., China) based on the sessile drop method using 2 mL of D.I. water droplets under ambient temperature and humidity. Measurements were taken until droplets were well settled on samples and repeated in triplicate, at six different positions per substrate type.

The surface topologies of pure PPS, and PPS/nano-HA powders were observed by field-emission scanning electron microscopy (FE-SEM, JSM-7500F, JEOL, Japan). Before observation, the samples were sputtered with gold for 60 s and examined at an accelerating voltage of 5 kV.

Water absorption assay of the PPS/nano-HA biocomposites was performed by incubating dry samples into D.I. water for 3, 5, and 7 days at 37 °C. At noted intervals, specimens were taken out, and any visible surface moisture was wiped off using filter papers. These samples were weighed using a digital balance (Jinghai Instruments Co., Ltd., Shanghai, China) with a precision of 0.1 mg. The water uptake percentage at any given time (W_t) in samples was determined from:

$$W_t\ (\%) = \frac{(M_t - M_0)}{M_0} \times 100\% \quad (2)$$

where M_0 is the initial weight of dry samples and M_t denotes the weight of samples after exposure in D.I. water at a certain point of time t. Six parallel specimens at each time point were tested to provide the average and standard deviation.

Mechanical property evaluation including ultimate tensile strength and bending strength of pristine PPS and PPS/nano-HA composites was performed by universal testing machine (AGS-J, Strider Instruments, Shanghai, China) at a loading velocity of 3 cm min^{-1}. Before measurement, the samples were cut to be 4 mm in thickness, 10 mm in width, and 6 mm in length for test. The elastic modulus and flexural modulus of samples were obtained from stress–strain curves. Six pieces of samples were used to improve the statistics.

The thermal analysis including thermogravimetry and differential scanning calorimeter (TG-DSC) was carried out to

Table 1 Synthesizing conditions for preparing different PPS/nano-HA biocomposites

Sample name	PPS content (wt%)	Nano-HA content (wt%)	Method
s-PPS_7/nano-HA_3	70	30	Solid–solid blending
s-PPS_6/nano-HA_4	60	40	Solid–solid blending
l-PPS_7/nano-HA_3	70	30	Liquid–liquid compounding
l-PPS_6/nano-HA_4	60	40	Liquid–liquid compounding

supply the information of phase transformation of the final composites. A small fragment weighing about 11 mg cut from the material was heated from 30 °C to 1000 °C with a heating rate of 10 °C min^{-1} under a nitrogen atmosphere.

2.5. Immersion test in SBF

The 1× SBF (Table S1†) was prepared by dissolving the following chemicals in the sequence of NaCl, $NaHCO_3$, KCl, $K_2HPO_4 \cdot 3H_2O$, $MgCl_2 \cdot 6H_2O$, $CaCl_2$, and Na_2SO_4 in D.I. water and buffering to pH 7.4 with $(CH_2OH)_3CNH_2$ (Tris) and 1 M HCl at 37 °C. Pure PPS and PSS/nano-HA samples were immersed in SBF solution at 37 °C in a static condition for 10 days. After soaking at scheduled time, the pH of the solution was monitored by a pH meter (Sartorius, pb-10, Germany) with an accuracy of ±0.02. Six samples in each stage were measured to provide an average and standard deviation.

2.6. Hemocompatibility assessments

2.6.1. Hemolysis test. Healthy New Zealand white rabbit (provided from Third Military Medical University, Chongqing, China) blood containing sodium citrate (3.8 wt%) in the ratio of 9 : 1 was taken and diluted with normal saline (4 : 5 ratio by volume). The PPS/n-HA biocomposite and pure PPS (Φ10 mm × 2 mm) was dipped in a standard tube containing 10 mL of normal saline that was previously incubated at 37 °C for 30 min. Then 0.2 mL of diluted blood was added to this standard tube, and the mixtures were incubated at 37 °C for 60 min per ISO 10993-4: 2002. As a negative control, 0.2 mL of diluted blood was again diluted with normal saline, and distilled water was added to a standard tube containing diluted blood, which served as a positive control. After the incubation, all the tubes were centrifuged for 5 min at 2500 rpm, and the supernatant was carefully removed and transferred to a new 96-well plate for spectroscopic analysis by an ultraviolet-visible (UV-VIS) spectrophotometer (WFJ7200, UNIC, USA) at 545 nm. Six pieces of samples were used to improve the statistics.

$$\text{Hemolysis} \quad (\%) = \frac{OD_{test} - OD_{blank}}{OD_{negative} - OD_{blank}} \times 100\% \qquad (3)$$

2.6.2. Dynamic clotting time. Dynamic blood coagulation estimates the release of hemoglobin from residual erythrocytes that remained free from entrapment during clot formation. Assays were conducted by recalcifying anticoagulated whole blood, as described previously with several modifications.[33,34] Typically, the PPS/nano-HA and PPS discs were placed in individual 100 mL beakers respectively and then pre-warmed in a water bath at 37 °C for 5 min. Subsequently, anticoagulated whole blood (0.2 mL) was dripped onto the surface of the materials and incubated at 37 °C for a further 5 min, after which $CaCl_2$ solution (25 μL of 0.2 mol L^{-1}) was dripped into the blood to initiate the coagulation cascade (time 0). The beakers were shaken for 1 min to mix the $CaCl_2$ uniformly with the blood. The covered beakers were heated to 37 °C for a predetermined time (5, 10, 20, 30, 40, 50, and 60 min). At the designated termination point, the beakers were removed from the water bath and shaken for 10 min following addition of 100 mL D.I. water to lyse the free erythrocytes. The absorbance of the supernatants at 540 nm using a UV-VIS spectrophotometer (UNIC) was determined. Since the signal was derived from that proportion of erythrocytes remaining free of clot entrapment, absorbance was inversely proportional to the size of the clots. The absorbance–time curve was constructed using the average values from six replicate experiments, with the use of silylated glass as negative control.

2.7. Cell culture and seeding

Human osteoblast-like MG-63 cells and murine fibroblast L929 cells obtained from American Type Culture Collection (ATCC, USA) were adopted for *in vitro* tests. Cells were cultured in high-glucose Dulbecco's modified eagle's medium (DMEM, Gibco, Carlsbad, Canada), supplemented with 10% fetal bovine serum (Gibco), 0.1 mg mL^{-1} streptomycin (Harbin pharmaceutical factory, China) and 100 U mL^{-1} penicillin (Harbin pharmaceutical factory) at 37 °C in humidified 5% CO_2 incubator (Heraeus, Germany). Prior to cell experiments, the studied materials were sterilized using an autoclave at 121 °C for 30 min, followed by thorough rinse with disinfected D-Hanks buffer. When reaching 70–75% confluence, cells were dissociated with trypsin–EDTA (Gibco), counted by hemocytometer and seeded onto samples. The medium was refreshed every 2–3 days.

2.8. Cytocompatibility evaluation of PPS/nano-HA biocomposites

2.8.1. Indirect cytotoxicity on extracts. Test on extracts was carried out in accordance with the instruction of ISO 10993-5: 2009. The extraction media of the PPS/nano-HA composite and pure PPS specimens were prepared using serum free cell culture medium (DMEM), with the extraction ratio (the ratio of specimen surface area to extraction medium) of 3 cm^2 mL^{-1}, and then incubated in a humidified atmosphere with 5% CO_2 at 37 °C for 72 h. Cell culture medium (DMEM) was used as a negative control. L929 fibroblast were incubated in 96-well cell culture plates (Corning, USA) at 1×10^3 cells per 100 μL in each well and incubated for 24 h to allow attachment. Then culture media were substituted by the extracts obtained from the studied materials and incubated for consecutive 5 days. The cell viability was quantified using cell counting assay kit-8 (CCK-8, Dojindo, Kumamoto, Japan), as detailed elsewhere, based on the measurement of mitochondrial activity. At desired time intervals of cultivation, the cell morphology was observed under an inverted optical microscope (IX70, Olmypus, Japan). Then, 20 μL of CCK-8 solution was added into each well for another 2 h incubation in the dark. Then 100 μL of supernatant from each well was transferred to fresh 96-well cell culture plates. The absorbance value of the supernatant optical density (OD value) for each group was measured with a multifunctional microplate reader (GENios, Tecan, Switzerland) at 570 nm. Each test was carried out in sextuplicate. The cytotoxicity was expressed as the relative growth rate (RGR) as follow, and the standard of cytotoxicity determined by RGR was shown in Table S2.†

$$\text{Cytotoxicity (RGR, \%)} = \frac{OD_{test} - OD_{blank}}{OD_{negative} - OD_{blank}} \times 100\% \quad (4)$$

2.8.2. Cell proliferation. MG-63 cells were adopted to evaluate the cell proliferation on the prepared biocomposite in this work. After cell counting, cells were exposed to the PPS/nano-HA and bare PPS surfaces in 48-well plates at a density of 5×10^3 cells per well, respectively. After incubating for 4 days, the viability of adherent cells was assessed by the same CCK-8 kit as per the aforementioned description, and six parallel experiments in each stage were performed.

2.9. Osteogenic potential studies of PPS/nano-HA biocomposites

2.9.1. Alkaline phosphatase activity. ALP activity of MG-63 on samples was assessed using an ALP assay reagent kit (Nanjing Jiancheng Bioengineering Institute, China). Histochemical assay of ALP was performed after 9 days of culture with PPS/nano-HA and pure PPS samples according to a modified Kaplow assay. Briefly, cells were washed with PBS (pH = 7.4), dried and fixed in ethanol at room temperature for 30 s. Fixed cells were incubated for 10 min at 37 °C in ALP incubating medium, and then counterstained in hematoxylin for 5 min. The grey value (GV) of staining results for each sample was captured through the medical image analysis software (Motic Images Advanced, Xiamen, China) under the same acquisition parameters. Hence, ALP activity was normalized and expressed as the average optical density (AOD) = lg 225 − lgGV. Six parallel measurements were used to provide an average and standard deviation.

2.9.2. Quantification of osteocalcin by ELISA. The contents of OCN of cells at different culture times (3, 7, 14, and 21 days) were detected using an OCN mouse enzyme-linked immunosorbent assay (ELISA) (Biomedical Technologies Inc. USA) in the light of the supplier's instructions. Data were measured photometrically at 450 nm and normalized by the established standard curve. Six parallel experiments in each stage were performed.

2.9.3. Cell mineralization. Mineralized nodule formation on samples was evaluated on day 14, 21 and 28 by staining with Alizarin Red S (ARS, 2 w/v%, Sigma-Aldrich), which bind specifically to calcium salts. Cells were rinsed with PBS buffer and fixed in 4% formalin for 30 min, followed by washing with D.I. water. Afterwards, ARS solution was added and incubated for 20 min at room temperature, and thoroughly rinsed with D.I. water to eliminate unbound stain. The number of calcium deposited on the substrates at projected area (magnification 400×) was counted under the optical microscope (IX70) from five different areas (up, down, left, and right) per sample, and six samples in each stage was used to improve the statistics.

2.10. *In vivo* experiments

The animal experimental protocol was approved by the Institutional Animal Care and Use Committee (IACUC) of Sichuan University (NO. SKLODLL2013A177). All experiments were performed in compliance with animal protection law of the People's Republic of China, and followed IACUC guidelines. All the animals were maintained on a normal, solid lab diet and regular tap water.

2.10.1. Skin irritation test. The extracts of the studied materials (Φ6 mm × 1 mm) were also performed following the instruction of ISO 10993-5: 2009. The extraction media was prepared using normal saline with the extraction ratio of 3 cm^2 mL^{-1}, and then incubated in a humidified atmosphere with 5% CO_2 at 37 °C for 72 h.

Nine Sprague-Dawley (SD) rats (provided from Third Military Medical University, half males and half females) aged 3 months and weighing about 200 g were randomly divided into two groups: PPS/nano-HA biocomposite, and bare PPS. After under general anesthesia (0.5% pentobarbital sodium, intravenous injection, 10 mL kg^{-1}), the rats were dehaired on the back, then 0.1 mL of extracts were injected into the dorsal subcutaneous bilateral area at three different points. After 1 and 3 days post-injection, the rats were dehaired again, and the erythema and dropsy area on the back were observed.

2.10.2. Acute toxicity evaluation. Nine SD rats were randomly assigned to three groups ($n = 3$) after one week of accommodation. Animals in the PPS/nano-HA and PPS groups were injected intraperitoneally (50 mL kg^{-1}) with the extract media of studied materials. Negative control was injected with an equal volume of physiological saline. The general conditions (the activity, energy, feces, behavior pattern, and other clinical signs), body weight, and mortality of all rats after administration were continuously recorded during the experiments. At the end of 3 days, all animals were killed through overdose anesthetics, and their livers and kidneys were excised and kept in 4% paraformaldehyde for histopathology examination. Sections (about 5 μm) of liver and kidney tissues embedded in paraffin wax were stained with hematoxylin-eosin (H&E) and then observed using an optical microscope (IX70).

2.10.3. Subcutaneous implantation. Subsequently, six SD rats were used to evaluate and compare the biological responses of surrounding tissues towards PPS plates, Ti mesh and PPS/nano-HA ones. The sample implants were sterilized prior to surgery for *in vivo* testing. After anesthetized, the rats were placed in a prostrate position with the dorsal skin shaved and disinfected. Afterward, an 8 mm longitudinal skin incision was made to expose the superficial plane of the deep fascia. A pocket was then built by blunt dissection with scissors in which one piece of aseptic implant was inserted. Lastly, each subcutaneous pocket was sutured using absorbable thread (PDS II, Ethicon). By repetition of this procedure, each animal received 6 implants (2 PPS, 2 Ti mesh and 2 PPS/nano-HA plates), and hence, a total of 36 implants (12 for each group) were inserted. Intramuscular injection of penicillin (5 mg kg^{-1}) was implemented for first 3 days post-operatively. After 1 month, the animals were euthanized, and the implants with surrounding tissues were harvested, fixed in 4% paraformaldehyde for 24 h, dehydrated in gradient ethanol solutions (50–100%), and then embedded after the inside implants were carefully removed. Six histological transverse sections (about 5 μm per section) for each sample were prepared, stained with H&E and

photographed under the optical microscopy (IX70) for evidence of inflammation. The images were analyzed using Nano Measurer 1.2 image analysis software (Jie Xu, Fudan University, China) to determine the thickness of the fibrotic capsule around each implant.

2.10.4. Rat calvarial defect model. For the assessment of bone regeneration, the calvarial defect model in another 36 SD rats was used. All rats were randomly assigned to three groups as PPS/nano-HA, pure PPS and surgical titanium (Ti) mesh control ($n = 6$ for each group). These rats were generally anesthetized and their skulls were sterilized with 75% ethanol and tincture of iodine. 6 mm critical-sized defects were created on the middle of skull using a dental trephine bur (NSK Surgic XT, Japan), and sterilized samples were employed to cover the defect. All rats were sacrificed at 4, 6 and 8 weeks after surgery.

2.10.5. Soft X-ray observation. After sacrifice, the rat bones were underwent radiographic analysis with soft X-ray (BJI-UZ, Beijing HSCreate Electronic equipment Co., Ltd., China). All specimens were exposed to X-ray under the same conditions (source voltage 70 kV, current 50 mA, powder 3.5 kW, exposure duration 0.1 s).

2.10.6. Histological analysis. The bone samples around the implants were harvested and fixed in 10% formalin for 24 h, dehydrated in gradient ethanol solutions (each concentration for 15 min). The samples were embedded in paraffin blocks, cut into about 5 μm sections using a microtome (Leica-2016, Germany), and the sections were then placed onto slide glasses. The nuclei of the samples were stained with hematoxylin solution, and the cytosols of the samples were stained with eosin solution for 5 min to observe bone ingrowth and integration with the host tissue under an optical microscopy (IX70).

2.10.7. RNA extraction and quantitative real-time PCR. After sacrifice at 4, 6 and 8 weeks, the osteotylus tissues adjacent to the implants were collected. The total mRNA was isolated from cells in tissues using TRIzol (Invitrogen, USA) and reverse transcribed into cDNA using a Revert Aid First Strand cDNA Synthesis Kit (Thermo, USA) as per the manufacturer's instruction. Then, quantitative real-time polymerase chain reaction (RT-PCR) analysis was conducted with SYBR Premix Ex Taq II Kit (Takara Biotechnology Co., Ltd., Dailian, China) on a RT-PCR machine (Thermo Fisher, USA). All were performed in triplicate and the expression of glyceraldehyde-3-phosphate dehydrogenase (GAPDH) was employed as house keeping gene. Primers (provided from Sangon Biotech, Shanghai, China) used in the present study were listed in Table S3.† Primer sets (10 mM final concentration for each primer) were used in a volume of 20 mL per tube. The thermal profile of the PCR was 50 °C for 2 min and 95 °C for 10 min, followed by 40 cycles at 95 °C for 5 s and 60 °C for 1 min. The cycle threshold values (Ct values) were applied to determine the fold differences by ΔΔCt method.

2.11. Statistical analysis

All the quantitative data were expressed as mean ± standard deviation. Statistical analysis was done using SPSS 10.0 software. One-way analysis of variance (ANOVA) or Student's *t*-test was used to determine the significant differences among the groups, and *p*-values less than 0.05 were considered statistically significant.

3. Results and discussion

3.1. Characterization of nano-HA crystals

The XRD pattern of the resulting powders was displayed in Fig. 1a. The Bragg diffraction peaks of the product, matched quite well with those of traditional nano-HA (PDF # 09-4032) at 2θ values of 25.9°, 31.7°, 32.9°, 39.6°, 49.4°, and 53.1°, which were indexed to (002), (211), (300), (222), (213), and (004) planes respectively,[35] proving the formation of nano-HA phase. Fig. 1b showed the FT-IR spectra of HA powders, also confirming the presence of an apatite phase. The typical broad peak at 3442 cm^{-1} and 1641 cm^{-1} were associated with the adsorbed water (H_2O). The weak band at 3576 cm^{-1} was attributed to the presence of OH^- group from nano-HA. Existence of CO_3^{2-} derived from atmosphere was recorded at around 1387 cm^{-1} (ν_3) and 871 cm^{-1} (ν_2), suggesting that trace amounts of PO_4^{3-} were partially substituted by CO_3^{2-} to form B-type carbon-substituted HA,[36] which was similar to the apatite found in the bone.[37] Moreover, several characteristic absorption peaks of PO_4^{3-} were also observed: the non-degenerate symmetric stretching mode ν_1 at 960 cm^{-1}, doubly degenerate bending mode ν_2 at about 464 cm^{-1}, the triply degenerate antisymmetric stretching vibration ν_3 at 1107 cm^{-1} and 1042 cm^{-1}, the triply degenerate vibration ν_4 at 608 cm^{-1} and 565 cm^{-1}.[35,38] Particularly, the peak at 960 cm^{-1} was a representative indication of crystalline HA.[39] The morphology and surface area of the nano-HA crystals was characterized by TEM and nitrogen adsorption experiment. The typical needle-like particles with a specific surface area value of 6.89 $m^2\ g^{-1}$ (Fig. S1†), which was the characteristic structure of nano-HA obtained from chemical precipitation process, were presented in Fig. 1c. Due to the high surface area and surface energy, the HA nanoparticles with a length of 82 ±

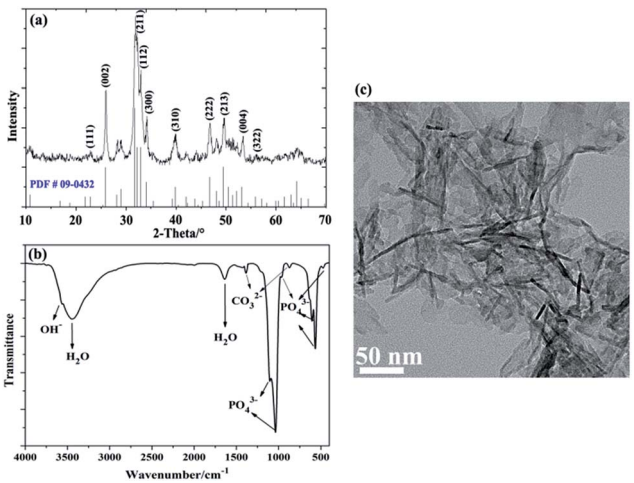

Fig. 1 Chemical constituent and morphology of nano-HA particles: (a) XRD pattern, (b) FT-IR spectra, and (c) TEM image.

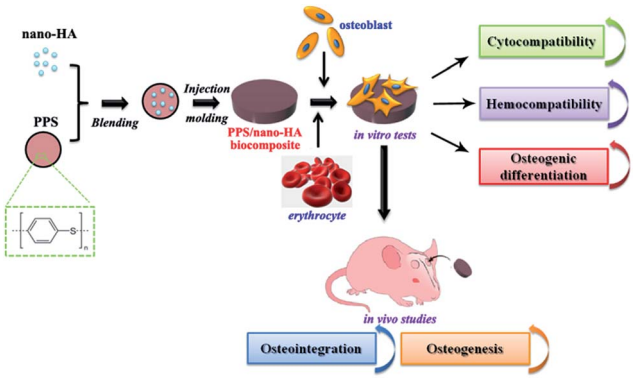

Fig. 2 Schematic illustration of preparation and *in vitro*/*in vivo* evaluation of the PPS/nano-HA biocomposite.

11 nm and a width of 9 ± 3 nm had a strong tendency to generate agglomerates.

3.2. Preparation and characterization of PPS/nano-HA composite

PPS is one a well-known semi-crystalline thermoplastic polymer for a set of outstanding traits, including quite high chemical resistance, low creep, reasonable cost allied with excellent mechanical properties analogous to PEEK.[40,41] So it could be explored to engender new hard tissue repair biomaterial, but yet suffers from bioinertness and defective osteogenesis. Besides, the current stiffness and elastic modulus of pure PPS are insufficient to replace natural bone. On the other hand, although nano-HA particles displayed similar physico-chemical features such as chemical composition, crystalline structure, and morphology with mineral nanocrystals in bone tissue, their extremely brittle nature may hamper their use for loading-bearing applications. Therefore, the HA nanoparticles were then doped with PPS matrix *via* compounding and injection-molding processes to overcome HA's mechanical weaknesses and improve PPS's osteogenesis for bone repair implant. The steps in fabricating and biologically evaluating our developed PPS/nano-HA bioactive composite were illustrated in Fig. 2.

To explore the alterations of chemical composition and morphology after the blending of nano-HA and PPS, the prepared PPS/nano-HA biocomposites *via* two different methods were characterized by FT-IR, contact angle goniometry, SEM, water uptake analysis, variation of local pH value as well as TG-DSC. The FT-IR spectra of various PPS/nano-HA biocomposites were depicted in Fig. 3a. Pure PPS matrix exhibited some feature peaks: the strong peak at 811 cm^{-1} originated from C–H out-of-plane bending vibration of benzene, and the bands at 3063 cm^{-1} corresponded to stretching vibration band of C–H. Three typical bands of C–C vibration at 1390 cm^{-1}, 1473 cm^{-1}, and 1572 cm^{-1} belonged to the in-plane stretching vibration of benzene. The FT-IR absorption peaks at 1004 cm^{-1} and 1087 cm^{-1} were ascribed to C=C in-plane bending vibration of benzene and C–S in-plane stretching vibration, respectively.[42,43] It was notable that the bands of P–O stretch and vibration at 558 cm^{-1}, 602

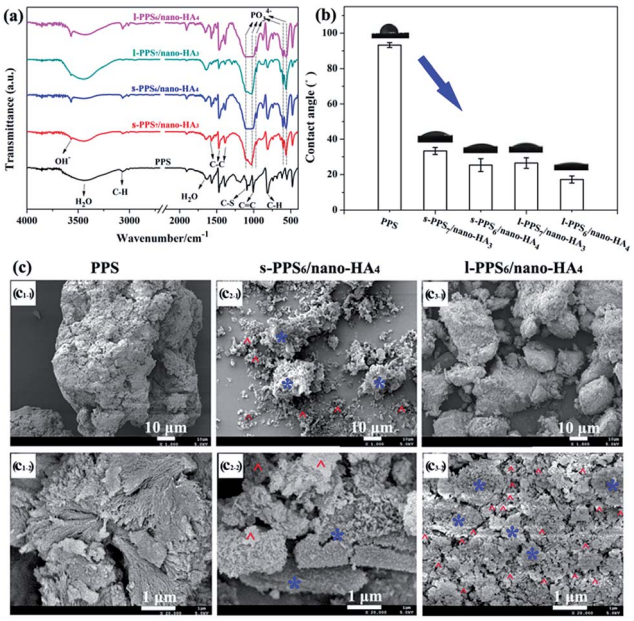

Fig. 3 FT-IR spectra (a) and water contact angle (b) of s-PPS/nano-HA and l-PPS/nano-HA binary composite. SEM images (c) of s-PPS_6/nano-HA_4 and l-PPS_6/nano-HA_4.

cm^{-1}, 961 cm^{-1}, 1035 cm^{-1}, and 1102 cm^{-1} resulted from the PO_4^{3-} group and the peak of OH^- group showed up in the s-PPS/nano-HA and l-PPS/nano-HA,[35,38] reflecting the compound of HA and PPS. Whilst the intensity of peaks from PO_4^{3-} groups for both s-PPS/nano-HA and l-PPS/nano-HA increased with nano-HA amount.

In biological systems, the hydrophilicity of the implant surface plays a fatal role in mediating cell adhesion and proliferation. The presence of nano-HA particles on PPS surfaces might help elevate the bioactive properties of the composite, especially the hydrophilicity. The wettability of bare and modified PPS was determined by contact angle measurements of sessile water drop. As presented in Fig. 3b, bare PPS substrate had hydrophobic feature with a contact angle of approximately 92° corresponding to the lowest surface hydrophilicity, owing to its hydrophobic aromatic ring and C–S functional groups. Numerous superhydrophobic materials, like polytetrafluoroethylene (PTFE),[44] polyvinylidene fluoride (PVDF),[45] and PEEK[5] were reported to display increased wettability when blended with nano-HA, owing to the hydrophilicity of OH^- group in HA crystals. Thereby, contact angle measurement showed that the introduction of HA nanoparticles significantly improved the hydrophilicity of PPS to a certain extent, with increase in HA concentration both for solid–solid blending and liquid–liquid compounding approaches. Moreover, compared with s-PPS_7/nano-HA_3 (33.3 ± 1.9°) and s-PPS_6/nano-HA_4 (25.1 ± 3.7°) composites, surface wettability of the corresponding l-PPS_7/nano-HA_3 (26.5 ± 3°) and l-PPS_6/nano-HA_4 (17.2 ± 2.3°) was enhanced at same nano-HA content, providing an indirect evidence for the more presence of HA on the outermost surface of l-PPS/nano-HA composite through liquid–liquid compounding process.

The effect of nano-HA and blend mode on the surface topology of PPS/nano-HA composite powders was examined by SEM. There were no detectable differences in the surface morphologies between PPS_7/nano-HA_4, and PPS_6/nano-HA_4 samples, therefore, PPS_6/nano-HA_4 as representative was observed under SEM. As shown in Fig. 3c, pure PPS powders possessed a rough surface morphology with petal shapes under high magnification. It could be seen that bulk PPS particles (*) and small HA powders (^) were visually separated in the s-PPS/nano-HA composite. Compared with s-PPS/nano-HA group, nonetheless, the bulk particles were comprised of PPS matrix and HA crystals. In the vision of high magnification, nano-HA particles (^) dispersed homogeneously in the compound powder and combined firmly with PPS matrix (*), suggesting that liquid–liquid compounding method was more beneficial to increase the dispersity and bonding strength of nano-HA in the compound than solid–solid blending approach.

Furthermore, the moisture absorption percentage of pure PPS and PPS/nano-HA samples within the initial 7 days was presented in Fig. 4a. The amount of water adsorption kept ascending quickly with the extension of time, except for pure PPS, which displayed no obvious water uptake during 7 days. The moisture is predominantly absorbed by composite component in the composites, because PPS matrix is water resistant. The numerous free hydroxyl (OH^-) groups present in the nano-HA crystals are responsible for forming hydrogen bonding with water molecules, and the water absorption of the composites hinges on the availability of free hydroxyl functions on the surface. Therefore, the percentage of water absorption on the biocomposite enhanced with the augmentation of nano-HA content. Additionally, the synthetic method also had a conspicuous influence on the moisture absorption of biocomposites. Clearly, at same nano-HA content, the water adsorption of l-PPS/nano-HA was substantially higher than that of s-PPS/nano-HA, and among them l-PPS_6/nano-HA_4 showed the best the water stored ability with 8.69 ± 0.83%. It could be explained by the better homogeneous dispersion of nano-HA in the composite prepared from liquid–liquid strategy. These results were in coincidence with the hydrophilicity test. The incorporation of nano-HA crystal and proper blending approach conferred inert PPS with strong bonding with water and good water holding function.

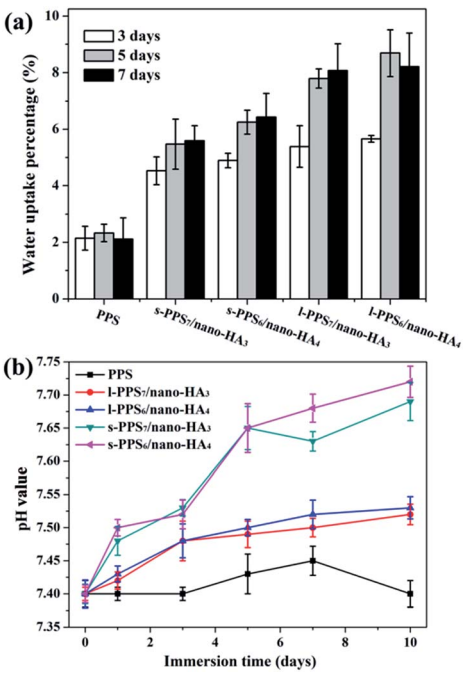

Fig. 4 Water uptake property (a) and variation of pH value (b) with soaking time in SBF for the pure PPS, and PPS/nano-HA biocomposite.

The local microenvironment of pH alteration resulted from materials degradation is an important parameter that should be considered, when designing materials for biomedical applications. The evolution of the pH values, hence, in SBF *vs.* soaking time for pure PPS and PPS/nano-HA biocomposites was shown in Fig. 4b. The pH values in SBF solution was improved, to different extents, for four PPS/nano-HA composites, whilst pure PPS exert no influence on the pH value maintaining at about 7.4 until 10 days. However, a drastic fluctuation in pH value increasing from 7.40 to 7.69–7.72 was seen in s-PPS/nano-HA composite owing to the partial ion exchange between H_3O^+ in SBF solution and Ca^{2+} cation from nano-HA on the surface. Moreover, the pH values of l-PPS/nano-HA exhibited a slight promotion from 7.40 to 7.52–7.53, and there was no evident difference in pH value between l-PPS_7/nano-HA_3 and l-PPS_6/nano-HA_4. The change of pH value for these PPS/nano-HA composites decreased in the order: s-PPS_6/nano-HA_4 > s-PPS_7/nano-HA_3 > l-PPS_6/nano-HA_4 ≥ l-PPS_7/nano-HA_3 > PPS. It was apparent that s-PPS/nano-HA groups induced more pH alteration in SBF than their counterpart (l-PPS/nano-HA) at same HA contents. This was because that weak binding between nano-HA crystals and PPS matrix through simple solid–solid blending contributed to rapid release of Ca^{2+}, and finally led to a serious fluctuation in pH value. Ca^{2+} ions, nonetheless, released slowly from the surface of l-PPS/nano-HA on account of homogeneous dispersion of nano-HA in compound generating alkalescence condition (pH = 7.52–7.53) and weak undulation in pH value. Some earlier studies, at the same time, confirm that excessive dissolved Ca^{2+} led to drastic alteration of the microenvironment combined with the deteriorated mechanical properties of implant materials, disruption in the activity of host cells and creating adverse effects on adjacent tissues.[46,47] In fact, tissue fluid (pH = 7.1–7.5) in human body is under a weak alkaline condition, and it is constantly circulating in the body to maintain homeostasis. And it was also verified that alkalescency derived from biomineralization was conducive to osteoblast proliferation and succedent osteogenic differentiation.[48,49] Local alkalescent microenvironment and weak fluctuation of pH after immersion of specimens in SBF solution confirmed that l-PPS/nano-HA composite had a good stability *in vitro*.

3.3. Mechanical properties of PPS/nano-HA composite

Current treatments of large-sized bone defects prevailingly rely on the use of metal implants made of Ti and Ti alloys. Nevertheless, the ultimate tensile strength of Ti alloys (over 900 MPa)

Table 2 Mechanical properties of the PPS/nano-HA composite with different nano-HA contents and synthetic methods

Sample name	Tensile strength (MPa)	Elastic modulus (GPa)	Bending strength (MPa)	Flexural modulus (GPa)
PPS	60.97 ± 2.32	2.78 ± 0.58	103.68 ± 1.67	3.29 ± 0.39
s-PPS_7/nano-HA_3	45.95 ± 2.20	3.72 ± 0.21	93.29 ± 4.16	5.16 ± 0.24
s-PPS_6/nano-HA_4	41.38 ± 1.71	4.29 ± 0.64	87.29 ± 3.18	6.45 ± 0.46
l-PPS_7/nano-HA_3	72.13 ± 3.79	4.74 ± 0.73	135.62 ± 4.53	6.89 ± 1.04
l-PPS_6/nano-HA_4	80.47 ± 3.38	6.10 ± 0.45	156.82 ± 5.27	8.37 ± 0.56

was approximately 6–20 times greater than that of cortical bones, which resulted in stress shielding. The use of materials stiffer than bony tissue leads to mechanical mismatch problems between the implant and the adjacent bone, where the integrity of the bone/implant interface may be compromised due to the resorption of bone tissue. Therefore, it is desired to fabricate novel material which mechanical performances of the repair material could be tailored to mimic human cortical bone avoiding stress shielding. Table 2 presented the mechanical properties of bare PPS and PPS/nano-HA composites with different contents of n-HA and synthetic methods. Obviously, extremely low elastic modulus (2.78 ± 0.58 GPa) and flexural modulus (3.29 ± 0.39 GPa) were detected in pristine PPS, while the s-PPS/nano-HA composite prepared from solid–solid blending exhibited a dramatic increase in elastic modulus and flexural modulus, but a reduce in tensile strength and bending strength as the nanoparticle concentration rose. With regard toward the l-PPS/nano-HA fabricated by liquid–liquid compounding, differing from s-PPS/nano-HA, the four mechanical indexes containing elastic modulus, flexural modulus, tensile strength, and bending strength were all improved with the n-HA content from 0 to 40 wt%, indicating enhancement in stiffness of the composites. Furthermore, it was remarkable that l-PPS/nano-HA composite, in contrast to s-PPS/nano-HA, displayed high mechanical properties at the same formulation, suggesting uniform decentralize of nano-HA and close linkage between nano-HA crystals and PPS matrix in the compound, contributing to improvement of mechanical properties. For developing a repairing prosthesis for bone tissue engineering, the material should be able to withstand dynamic mechanical loading under *in vivo* conditions. From the mechanical testing results, the composites prepared *via* liquid–liquid compounding method in our study harbored an elastic modulus in the range of 4–6 GPa, which endowed them with sufficient mechanical strength for load-bearing orthopedic and neurosurgical applications. Moreover, the enhanced elastic modulus was also believed to have a positive effect on the osteogenic differentiation of bone cells.[50] It was expected that the l-PPS/nano-HA nanocomposites, especially for l-PPS_6/nano-HA_4, with such mechanical properties had a promising prospect used as load-bearing implant material.

At last, the representative curves of TG and DSC analysis for the l-PPS_6/nano-HA_4 composite were depicted in Fig. 5. It showed that the final PPS/nano-HA had a two-step thermolysis. The sharp weight loss (about 37.22%) in a range of 400–650 °C was ascribed to thermal degradation and pyrolyzation of PPS

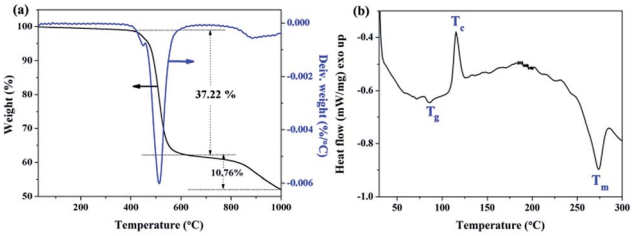

Fig. 5 TG-DSC analysis of the final l-PPS_6/nano-HA_4 composite.

molecules. There was a slow weight loss with 10.76% located at 650–1000 °C, probably corresponding to the release of OH^- ions from the decomposition of HA, leaving oxyapatite (OAP) behind. According to the DSC results, the glass transition temperature (T_g), thermal crystallization temperature (T_c), and melting temperature (T_m) of new l-PPS_6/nano-HA_4 binary composite were 85.6 °C, 115.2 °C, and 273.5 °C respectively, which was similar to those of pure PPS.[18]

3.4. Blood compatibility of PPS/nano-HA biocomposite

Hemocompatibility assessments including hemolysis test and dynamic blood coagulation testing were also evaluated in the present study, because for potential blood-contacting bone implant, the interplay between blood and biomaterials could affect bone formation and healing. The degree of hemolysis is a sensitive indicator of the extent of damage to erythrocytes. The degree of hemolysis in the presence of l-PPS_6/nano-HA_4 was 1.66 ± 0.29%, way below the safety-threatening threshold of 5%, suggesting that l-PPS_6/nano-HA_4 biocomposite provided an acceptable level of hemolysis. It was noteworthy, nonetheless, that the hemolysis rates for bare PPS sample (6.43 ± 0.76%) stayed higher than 5%, indicating that it had a risk of accelerating thrombosis and leading to further coagulation. The dynamic blood clotting time is an *in vitro* test that measures the degree of activation of intrinsic coagulation factors when surfaces interact with blood ("contact activation"). A curve providing a gentle slope usually implied low procoagulant properties in the implanted material.[51,52] Fig. 6 presented that the similar curves for l-PPS_6/nano-HA_4 biocomposite and silylated glass (negative control), with both presenting slow and smooth downward inclination with coagulation time beyond 60 min; nevertheless, unmodified PPS displayed sharp blood coagulation cascade with procoagulant time at 20 min. Endosseous implants initially come into contact with blood. The interactions between blood and bone implants have

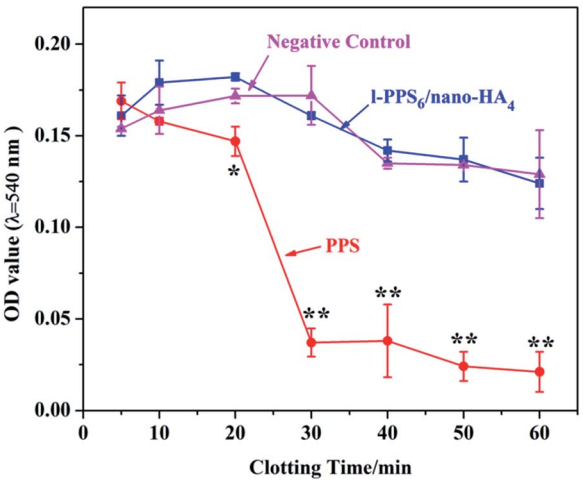

Fig. 6 Curves of dynamic clotting time of pure PPS and l-PPS_6/nano-HA_4 biocomposite with silylated glass as negative control. * represents $p < 0.05$, ** represents $p < 0.01$ compared with l-PPS_6/nano-HA_4 and negative group.

a momentous impact on subsequent bone healing events in the peri-implant healing compartment. The finding of the study indicated that l-PPS_6/nano-HA_4 biocomposite with preferable hemocompatibility could have better potential to be used for orthopaedic implants.

3.5. Cell toxicity

A good biocompatibility with the surrounding tissue cells is usually expected for implantable materials, therefore, the cytotoxicity of PPS/nano-HA biocomposite was probed by CCK-8 assay on the murine fibroblast L929 cells, which was widely used for cytotoxicity evaluation of biomaterials. Fig. 7a depicted

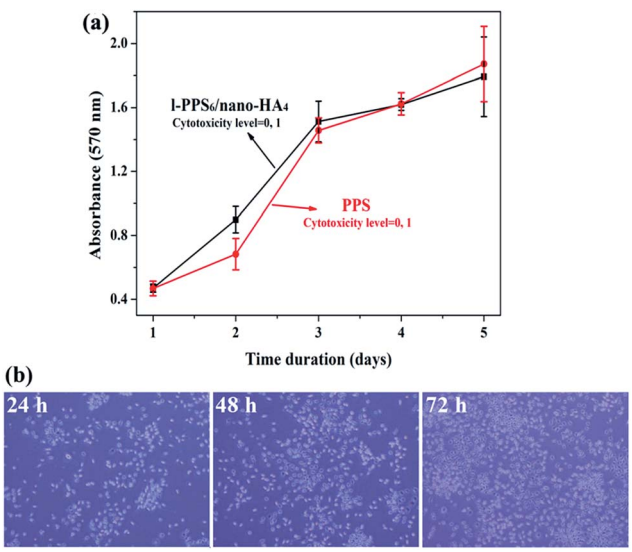

Fig. 7 (a) Indirect cell viability of L929 cells cultured in extract of the bare PPS and l-PPS_6/nano-HA_4 biocomposite, and (b) the optical microscope images of cells cultured in extract of the l-PPS_6/nano-HA_4 biocomposite.

the cell viability cultured in extracts of pristine PPS and l-PPS_6/nano-HA_4 for sequential 5 days, with pure DMEM media as control. It could be found that the OD value increased with time when L929 cells were co-cultured with the two extracts attested that PPS-based materials did not induce cytotoxic effect on cells. In addition, no significant differences in cell viabilities difference between l-PPS_6/nano-HA_4 and PPS, representing a similar non-toxicity feature. During 5 days of culture, the proliferation of L929 cells cultured in l-PPS_6/nano-HA_4 surface varied between 95.3% (day 5) and 103.56% (day 3), corresponding to the cytotoxicity level of 0 or 1 per the standard in Table S2.† Due to excellent biocompatibility and high mechanical behaviors, titanium and PEEK are two more used biomaterials as orthopedic implant. The cell viability and cytotoxicity level of the PPS-based materials were comparable to that of pure titanium (89–98% RGR)[6,53] and PEEK (85–96% RGR, those data from previous literature)[6,54] because of the bioinertness of these biomaterials, implying PPS-based materials had similar cytocompatibility to titanium and PEEK. These phenomena were further verified by optical microscopic observation. The morphologies of L929 cells cultured in extraction media from the l-PPS_6/nano-HA_4 group displayed healthy spindle-like shape, and the amount of cells rose with the extension of culture time (Fig. 7b), suggesting that l-PPS_6/nano-HA_4 composite imposed no suppression on the growth of cells. Good correspondence could be found between the direct observation and the indirect cell viability evaluation.

3.6. Cell proliferation and osteogenic differentiation *in vitro*

Initial cell adhesion is usually responsible for cellular functions and eventual tissue integration, while cell proliferation is closely correlated with the amount of new bone formation. Better cell proliferation probably produces a larger mass of bone tissues around the implant.[55] To further explore MG-63 cells proliferation on PPS/nano-HA composite in the context of bone tissue engineering, CCK-8 assay was carried out. According to the viability data in Fig. 8a, all studied materials exhibited good time-dependent cell activity. Although cells at day 1 displayed no statistical difference among groups, nano-HA doped PPS possessed higher cell multiplication than pure PPS and kept better viability from day 2 to day 4, indicating that the exposure of nano-HA might have a positive impact on the cytocompatibility and improving the bioactivity of PPS materials. The osteogenic differentiation activity of cell to the bio-interfaces, as far as bone-repair biomaterials concerned, is a key event in bone formation. Among the major osteogenic hallmarks, the up-regulation of ALP activity is a central event occurring during the early time points of osteogenesis.[56] *In vitro* ALP activities of MG-63 cells cultivating with pure PPS and PPS/nano-HA biocomposite were evaluated at 1, 4, 7, and 14 days. As illustrated in Fig. 8b, when cells were cultured on PPS/nano-HA, the ALP activity expression was pronouncedly higher compared with that for pure PPS, whose ALP values almost kept unchanged.

Concomitantly, OCN secretion and mineral deposition, being connatural characteristics of bone-like structures, were

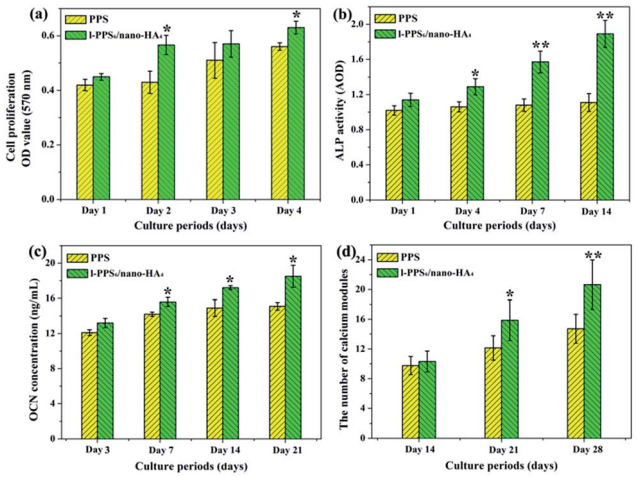

Fig. 8 The cell proliferation and osteoblastic functions of MG-63 co-cultured with the pristine PPS and PPS/nano-HA biocomposite: (a) cell proliferation, (b) ALP activity, (c) the amount of secreted OCN quantified by ELISA, and (d) the number of calcium modules stained by ARS. * represents $p < 0.05$, ** represents $p < 0.01$.

estimated as osteogenic markers at the late stage (Fig. 8c and d). OCN is regarded as the most specific marker for the mature osteoblast and mineralization during the course of osteogenesis, and it reaches the maximum expression during mineralization and accumulates in the mineralized bone due to its high affinity to HA crystals.[57] As the osteogenic culture of MG-63 cells progressed to 21 days, cells started to aggregate together and form bone-like structures stained by ARS. Evidently, a drastic enhancement in the number of nodules and the amount of OCN protein were detected at most time points (14, 21 and 28 days) on PPS/nano-HA biocomposite compared with those on pure PPS, due to addition of nano-HA underlining the role of nano-HA crystals in the enhancement of osteogenic differentiation efficiency. As mentioned above, nano-HA crystals have been accepted to greatly up-regulate biological markers during osteogenesis and enhance osteogenic differentiation of bone cells,[28,58] therefore facilitating the formation of bone. Besides that, the Ca ion released from nano-HA have been shown to stimulate osteoblast proliferation and differentiation by changing the expression of specific Ca^{2+} channel isoforms on osteoblasts.[59] Overall, results from cell proliferation, ALP activity, calcium nodule deposits and OCN expression have clearly showcased that our developed PPS/nano-HA possessed robust osteoinductive capacity, and the addition of nano-HA has endowed bioinert PPS with both outstanding osteo-compatibility and osteogenesis potential *in vitro*.

3.7. *In vivo* biocompatibility evaluation

To verify the biocompatibility of l-PPS_6/nano-HA_4 biocomposite for clinical use, it is crucial to know its *in vitro* responses, therefore, the *in vivo* biocompatibility assessments including skin irritation test, acute toxicity evaluation and subcutaneous implant experiments were performed in the present work. First, a skin irritation test was conducted to determine whether l-PPS_6/nano-HA_4 biocomposite invoked inflammatory and allergic reactions. Although there was a little erythema on both dorsal areas of rats at the 1st day after injection of PPS and l-PPS_6/nano-HA_4 biocomposite extraction, after 3 days, the erythema disappeared and none of the tested parts of white rats treated with the extract medium displayed edema reactions (Fig. S2a†), implying that PPS-based materials were not irritant or traumatic to the skin. No death occurred during the whole 3 day observation period, and no toxic response was found in rats. The animals displayed normal energy, normal behavior, free movement, and shining hair. The animals' feces were in regular form and normal color, without mucus, pus, or blood. After sacrifice, no macroscopic pathological alterations and histopathological lesions attributed to the extracts of PPS and biocomposite were found in any rats at necropsy. Fig. S2b† presented the light microscopic image of the liver and kidney treated with the extracts. The classic structure of liver lobule with central vein was delineated, and no hepatocellular degeneration or necrosis was found. From the light micrograph of rat kidney, many renal tubes with normal shape were observed, with no degeneration, bleeding, or necrosis. In summary, these results showed that both PSS and l-PPS_6/nano-HA_4 materials had no short-term acute systemic toxicity, reflecting it might serve as a safe candidate for its potential applications in biomedicine fields.

3.8. *In vivo* bone formation assessments

3.8.1. Subcutaneous implant experiments. In order to further explore tissue responses *in vivo*, subcutaneous implant experiments were designed and conducted. Histological sections at 30 days post-implantation were given in Fig. 9a–c, with Ti mesh and pure PPS as control. The "encapsulation" of the materials, a typical foreign–body reaction, was seen in all groups. The collagen fibrils of capsule wall tightly jointed with contiguous subcutaneous tissue. No significant signs of macrophage activation, inflammation, hemorrhage, necrosis, or purulency after 30 days' implantation in the ambient connective tissues were found, an implication of adverse reactions. Only a few fusiform fibroblasts, neutrophil, and polykaryocyte existed at the implant–tissue interface in a fast healing process. Further, the capsule thickness was used as a quantitative measure (Fig. 9d). Apparent significant discrepancy was found for the amount of fibroblasts among the three groups. It was obvious that the average thickness of the fibrous membrane for PPS/nano-HA was 156.02 ± 10.48 μm, much thinner than that for PPS and Ti mesh with 85.91 ± 5.18 μm and 36.05 ± 3.62 μm, respectively. Altogether, compared to PPS and Ti mesh, the PPS/nano-HA surface was likely to evoke lower acute foreign-body reaction.

3.8.2. Calvarial defect repairing observation. Natural bone is a complex material that mainly composed of cells, collagen matrix, polysaccharides, and nanoscale HA minerals. Inspired by the constituents of the natural bone, previous studies have used a crowd of polymer/nano-HA compounds to fabricate bone-repairing scaffolds, such as PEEK/nano-HA,[5,60] poly-L-lactide/nano-HA (PLLA/nano-HA),[61] collagen/nano-HA,[62] PA66/

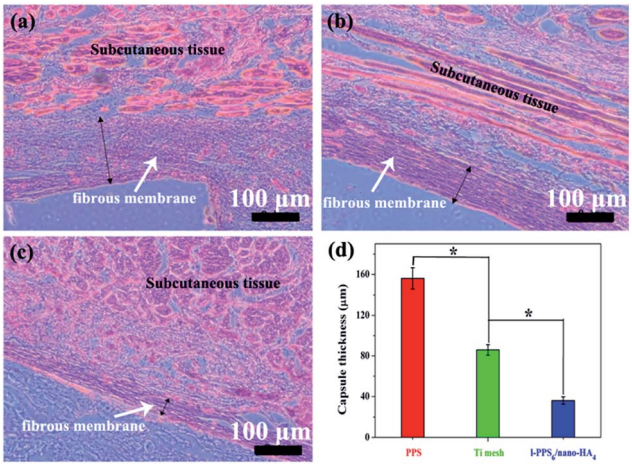

Fig. 9 Representative H&E stained images of soft tissues contacted with the sample surfaces following 30 d subcutaneous implantation: (a) pure PPS, (b) Ti mesh, and (c) l-PPS_6/nano-HA_4; (d) results of the histological analysis of capsule thickness. * represents $p < 0.05$.

nano-HA,[31] ultrahigh molecular weight polyethylene/nano-HA (UHMWPE/nano-HA)[63] and so on. Yet the popular high-performance engineering plastic, PPS, has not been exploited as hard tissue implant for bone substitution. So what interests us is how the PSS and PPS/nano-HA interplay with bone tissue, which as far as we know, has never been researched. We created critical-sized defects on rats (Fig. S3†), filled three types of materials (PPS, Ti mesh, and l-PPS_6/nano-HA_4) into the defects, and first analyzed calvarial bone specimens by soft X-ray eight weeks post-surgery. Representative X-ray images of three implants from frontal and lateral cephalometrics were displayed in Fig. 10a. Because of the radiolucency of PPS, the bone recovery around the implant can be readily probed by X-ray examination; however, white shadow was evident in Ti implant due to the radiopacity of metal alloys. The bone resorption and looseness of all implants after recovery were not seen showing good bind to bony tissue as presented in Fig. 10a.

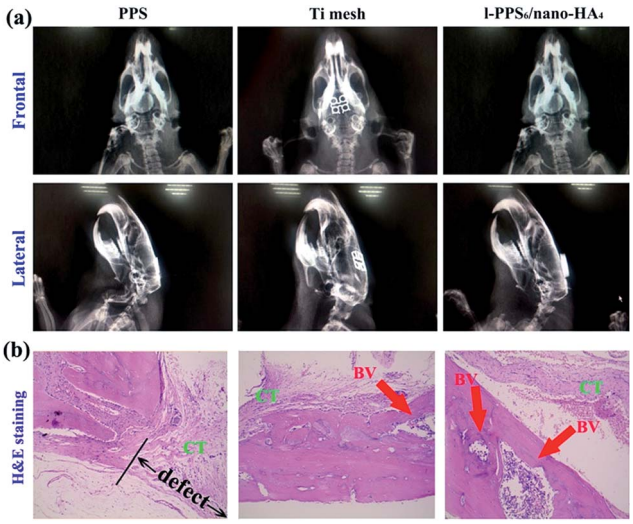

Fig. 10 (a) Soft X-ray images of rat cranial defects implanted with different implants and (b) H&E staining views of the sections of calvarial defects 8 weeks post-surgery. BV, blood vessel; CT, connective tissue.

Histological analysis was used to observe interactions between host tissue and implanted biocomposite at defect sites. As illustrated in Fig. 10b, we only find limited newly-formed osteotylus at the periphery of the defect and a few inflammatory cell infiltration, but a plentiful of fibrillar connective tissue filled the defect for PPS group at 8 weeks after implantation. In Ti mesh-implanted group, Ti mesh was encapsulated with host cells and more organized tissue regeneration around the defect sites were detectable than those in the PPS-implant group. In mineralized tissue, the process of angiogenesis is a prerequisite for normal osteogenesis. During bone repair angiogenesis precedes osteogenesis, since newly formed vessels drive the orientation of bone microcolumns.[64] In reconstructive orthopaedic surgery, therefore, adequate blood supply is necessary for bone re-built and regeneration. As shown in Fig. 10b, blood vessels infiltrated throughout the defects in the two implanted materials groups, but the highest concentration of blood vessels was found in the PPS/nano-HA biocomposite. Nanocrystalline HA has been proved to promote angiogenesis *via* up-regulation of fibroblast growth factor 2 (FGF-2).[65] One of the interesting results was that rats in the PPS/nano-HA-implanted group showed compact *de novo* bone, better bone healing, and regeneration of blood vessels (red arrow) in the newly-formed bone tissue. These results demonstrated that the quality of newly formed bone in contact with the implants of l-PPS_6/nano-HA_4 biocomposite group was drastically higher than that for bare PPS group. It seemed no significant discrepancy in bone healing and repairing between Ti mesh and l-PPS_6/nano-HA_4 biocomposite. It has been proved in vast previous literature that nano-HA modification of PEEK and Ti implants surfaces exhibited a prominently elevation in osteogensis-related gene expression levels and also exhibit higher degrees in the newly bone reconstruction.[66,67] When PPS/nanoHA is in contact with bone after implantation, the exposure of nano-HA inevitably promotes the growth of osteoblasts and accelerates angiogenesis, resulting in bone formation. The results are closely correlated with osteoblast proliferation and differentiation *in vitro* as well. Thus, the PPS polymer after blending nano-HA crystals not only positively affects the osseointeration between implant and bone but also enhances bone maturation surrounding the implant.

3.8.3. Quantitative real-time PCR. Cells enable to sense and respond to the changes from biochemical/biophysical stimuli from surrounding environment, triggering a cascade of intracellular events regulating gene expression associated with cell differentiation. An in-depth study on the gene expression at transcript level is instrumental to better understand the cellular/tissue interactions with composites and their subsequent effect on biological functions related to osteogenic differentiation. Therefore, we further conducted gene expression study for the cells derived from adjoining tissue contacted with composite implants, and monitored the changes in the expression of some osteo-specific and osteo-related genes encoding ALP, Col1α1, OCN, IGF-1, and TGF-β at 4, 6, and 8

weeks. ALP, which is a membrane-bound enzyme, plays an essential role in the mineralization of bone matrix *via* hydrolysis of organic phosphates. Col1α1 gene is an osteo-special marker expressed during the later period, which is involved in the biosynthesis of the extracellular matrix (ECM).[68] Of all the osteo-related genes, OPN, having a high affinity for HA, plays an imperative role in the process of bone mineralization and calcification.[57] For all groups, the expression peak of ALP and Col1α1 were the focus on week 4 and that of OCN located on week 8. As depicted in Fig. 11, cells with PPS implant expressed the least amount of all bone-related genes at every time point, indicating no osteoinductive property. Whereas stronger mRNA expression of ALP, Col1α1 and OCN were founded in Ti mesh groups in comparison to pure PPS, although the ALP expression showed no difference statistically at week 8. Simultaneously, the higher expression levels of three genes indicated that osteoblastic differentiation happened and more actively on l-PPS_6/nano-HA_4 than those on pure PPS and typical Ti mesh. On the other hand, several growth factor markers are characteristic of differentiated osteoclasts including Insulin-like growth factor 1 (IGF-1) and transforming growth factor beta 1 (TGF-β1). Among them, IGF-1 is known to stimulate the replication of osteoblasts proliferation and the synthesis of bone matrix *in vivo*.[69] TGF-β1 regulates different cell types directly involved in bone remodeling and fracture healing.[70] It was a finding that mRNA levels of IGF-I expression were up-regulated in both Ti mesh and PPS/nano-HA biocomposite at 6 and 8 weeks, but no significant changes between the two groups. Nonetheless, the fold change in expression of TGF-β1 for Ti mesh was more than of PPS substrates. Tissue subjected to l-PPS_6/nano-HA_4 biocomposite possessed the highest up-regulation in TGF-β1 expression (6.57 folds at week 4, 2.19 times at week 6, and 9.07 times at week 8 compared with that of pure PPS). There data all disclosed that these osteogenesis-related expressions of mRNA when tissue responded to l-PPS_6/nano-HA_4 group significantly outmatched those on pure PPS and traditional Ti implant, which showed the maximal expression among groups, demonstrating promoted ossification *in vivo*. To our delight, *in vivo* tests clearly demonstrated that our developed HA-doped PPS biocomposite held the superior ability to bond with host bones and substantially boosted osseointegration and bone-forming capability thereby boding well for orthopedic, craniomaxillofacial and dental applications.

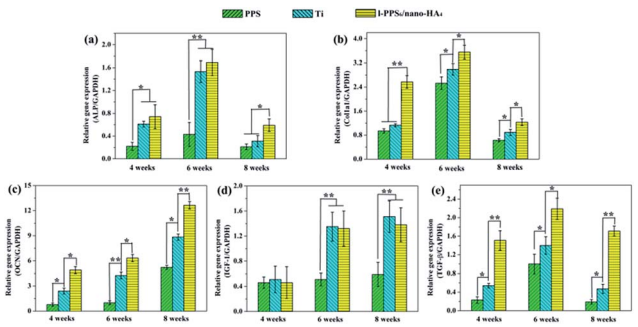

Fig. 11 Real-time PCR detection of osteogenesis-related genes expression encoding ALP (a), Col1α1 (b), OCN (c), IGF-1 (d), and TGF-β (e) of the cells originated from tissue contacted with pure PPS, Ti mesh and l-PPS_6/nano-HA_4 biocomposite for different weeks. * represents $p < 0.05$, ** represents $p < 0.01$.

4. Conclusion

In this paper, a unique PPS-based bioactive composite, PPS/nano-HA, was successfully developed through a process of compounding, and injection-molding, and its chemical constitutions, mechanical properties and biological performances were systematically evaluated both *in vitro* and *in vivo*. The mechanical property assessments proved that the elastic modulus of PPS/nano-HA samples was closer to that of human cortical bones. Cell experiment results demonstrated that the PPS/nano-HA composite was found to promote cell proliferation, osteogenic differentiation with higher ALP activity, and increased OCN secretion and calcium nodule-formation compared with bare PPS. More importantly, in the rat cranial defect implantation model, preferable tissue biocompatibility, better osteointegration, and accelerated osteogenesis could be observed around the PPS/nano-HA biocomposite implants *in vivo* than pure PPS and typical Ti mesh based on soft X-ray observation, histological analysis, and real-time PCR. This is the first time investigating the possibility of PPS and its composite as potential biomaterials. As consequence, our findings provide preliminary insights into the development of novel PPS-based biomaterials used in many challenging orthopedic/dental tissue engineering applications and enriched the library of PPS application in health issues.

Acknowledgements

This work was supported by the Natural Science Foundation of China (Grant 51173210), and the Fund of Health Department of Sichuan Province (No. 110467). Y. Deng and Y. Ma contributed equally.

References

1 M. Navarro, A. Michiardi, O. Castaño and J. A. Planell, *J. R. Soc., Interface*, 2002, **5**, 1137.
2 E. Gentleman, R. J. Swain, N. D. Evans, S. Boonrungsiman, G. Jell, M. D. Ball, T. A. Shean, M. L. Oyen, A. Porter and M. M. Stevens, *Nat. Mater.*, 2009, **8**, 763.
3 A. Dalal, V. Pawar, K. McAllister, C. Weaver and N. J. Hallab, *J. Biomed. Mater. Res., Part A*, 2012, **100**, 2147.
4 T. A. Schildhauer, E. Peter, G. Muhr and M. Köller, *J. Biomed. Mater. Res., Part A*, 2009, **88**, 332.
5 L. Wang, S. He, X. Wu, S. Liang, Z. Mu, J. Wei, F. Deng, Y. Deng and S. Wei, *Biomaterials*, 2014, **35**, 6758.
6 K. B. Sagomonyants, M. L. Jarman-Smith, J. N. Devine, M. S. Aronow and G. A. Gronowicz, *Biomaterials*, 2008, **29**, 1563.
7 A. H. C. Poulsson, E. David, Z. Stefan, C. Karin, S. Christoph, A. Yash, N. Dirk, W. Joanne and R. G. Richards, *Biomaterials*, 2014, **35**, 3717.

8 L. Ouyang, Y. Zhao, G. Jin, L. Tao, J. Li, Y. Qiao, C. Ning, X. Zhang, P. K. Chu and X. Liu, *Biomaterials*, 2016, **83**, 115.
9 A. Xu, L. Zhou, Y. Deng, X. Chen, X. Xiong, F. Deng and S. Wei, *J. Mater. Chem. B*, 2016, **4**, 1878.
10 X. Wang, T. Lu, J. Wen, L. Xu, D. Zeng, Q. Wu, L. Cao, S. Lin, X. Liu and X. Jiang, *Biomaterials*, 2016, **83**, 207.
11 L. Tao, W. Jin, Q. Shi, H. Cao, C. Ning, X. Pan, X. Jiang, X. Liu and P. K. Chu, *Biomaterials*, 2015, **51**, 173.
12 M. G. Garrell, B. M. Ma, A. J. Shih, E. Lara-Curzio and R. O. Scattergood, *Mater. Sci. Eng., A*, 2003, **359**, 375.
13 W. Luo, Q. Liu, Y. Li, S. Zhou, H. Zou and M. Liang, *Composites, Part B*, 2016, **91**, 579.
14 S. M. Kurtz and J. N. Devine, *Biomaterials*, 2007, **28**, 4845.
15 J. M. Toth, W. Mei, B. T. Estes, J. L. Scifert, H. B. S. Iii and A. S. Turner, *Biomaterials*, 2006, **27**, 324.
16 E. Alonso-Rodriguez, J. L. Cebrián, M. J. Nieto, J. L. Del Castillo, J. Hernández-Godoy and M. Burgueño, *Journal of Cranio-Maxillofacial Surgery*, 2015, **43**, 1232.
17 A. G. Kulkarni, H. T. Hee and H. K. Wong, *Spine J.*, 2007, **7**, 205.
18 Y. Guo and R. D. Bradshaw, *Polymer*, 2009, **50**, 4048.
19 A. M. Diez-Pascual, *Manufacturing of Nanocomposites with Engineering Plastics*, 2015, 127.
20 S. Pappadà, A. Salomi, J. Montanaro, A. Passaro, A. Caruso and A. Maffezzoli, *Aerosp. Sci. Technol.*, 2015, **43**, 314.
21 M. Kikuchi, Y. Koyama, T. Yamada, Y. Imamura, T. Okada, N. Shirahama, K. Akita, K. Takakuda and J. Tanaka, *Biomaterials*, 2005, **25**, 5979.
22 Y. Takahashi, M. Yamamoto and Y. Tabata, *Biomaterials*, 2005, **26**, 3587.
23 N. T. Khanarian, N. M. Haney, R. A. Burga and H. H. Lu, *Biomaterials*, 2012, **33**, 5247.
24 Y.-P. Guo, J.-J. Guan, J. Yang, Y. Wang, C.-Q. Zhang and Q.-F. Ke, *J. Mater. Chem. B*, 2015, **3**, 4679.
25 X. Wu, X. Liu, J. Wei, J. Ma, F. Deng and S. Wei, *Int. J. Nanomed.*, 2012, **7**, 1215.
26 R. D. Santis, M. Catauro, L. D. Silvio, L. Manto, M. G. Raucci, L. Ambrosio and L. Nicolais, *Biomaterials*, 2007, **28**, 2801.
27 M. J. Olszta, X. Cheng, S. J. Sang, R. Kumar, Y. Y. Kim, M. J. Kaufman, E. P. Douglas and L. B. Gower, *Mater. Sci. Eng., R*, 2007, **58**, 77.
28 H. Yang, H. Zeng, L. Hao, N. Zhao, C. Du, H. Liao and Y. Wang, *J. Mater. Chem. B*, 2014, **2**, 4703.
29 K. Yano, T. Namikawa, T. Uemura, M. Hoshino, S. Wakitani, K. Takaoka and H. Nakamura, *J. Orthop. Sci.*, 2012, **17**, 484.
30 L. Hua, W. X. Guo, Y. F. Wang, S. Z. Hong, X. Si, W. Yan, B. C. Heng, R. A. Cheng, H. Z. Gang and H. X. Ding, *Biomaterials*, 2015, **49**, 103.
31 H. Wang, Y. Li, Y. Zuo, J. Li, S. Ma and L. Cheng, *Biomaterials*, 2007, **28**, 3338.
32 J. Li, Y. Man, Y. Zuo, L. Zhang, C. Huang, M. Liu and Y. Li, *J. Biomater. Sci., Polym. Ed.*, 2011, **22**, 263.
33 L. Xie, H. Yu, W. Yang, Z. Zhu and L. Yue, *J. Biomater. Sci., Polym. Ed.*, 2016, **27**, 1.
34 F. Nie, Y. Zheng, Y. Wang and J. Wang, *J. Biomed. Mater. Res., Part B*, 2014, **102**, 221.
35 Q. Li, M. Li, P. Zhu and S. Wei, *J. Mater. Chem.*, 2012, **22**, 20257.
36 J. Ryu, S. H. Ku, H. Lee and C. B. Park, *Adv. Funct. Mater.*, 2010, **20**, 2132.
37 Y. Deng, Y. Sun, X. Chen, P. Zhu and S. Wei, *Mater. Sci. Eng., C*, 2013, **33**, 2905.
38 M. C. Chang and J. Tanaka, *Biomaterials*, 2002, **23**, 4811.
39 A. Antonakos, E. Liarokapis and T. Leventouri, *Biomaterials*, 2007, **28**, 3043.
40 H. Quan, G. J. Zhong, Z. M. Li, M. B. Yang, B. H. Xie and S. Y. Yang, *Polym. Eng. Sci.*, 2005, **45**, 1303.
41 L. G. Xia, A. J. Li, W. Q. Wang, Q. Yin, H. Lin and Y. B. Zhao, *J. Power Sources*, 2008, **178**, 363.
42 D. Zhang, H. Yao, D. Zhou, L. Dai, J. Zhang and S. Yuan, *Polym. Adv. Technol.*, 2014, **25**, 1590.
43 G. Miao, Z. Yu, Q. Wu and Y. Chen, *Eur. Polym. J.*, 1997, **33**, 1401.
44 N. L. de Macedo, L. G. de Macedo, F. S. Matuda, S. M. Ouchi, A. S. Monteiro and Y. R. Carvalho, *South Braz. Dent. J.*, 2003, **14**, 119.
45 J. Sun, Z. Cao and L. Wu, *Colloids Surf., B*, 2015, **126**, 265.
46 X. Lu, H. Yu, Y. Deng, W. Yang, L. Li and L. Qin, *Mater. Sci. Eng., C*, 2016, **59**, 1007.
47 S. Yamada, D. Heymann, J. M. Bouler and G. Daculsi, *Biomaterials*, 1997, **18**, 1037.
48 L. Fei, C. C. Wang, X. Yang, K. Lin, C. Jiang and S. Jiao, *J. Biomed. Mater. Res., Part B*, 2012, **100**, 1237.
49 W. Zhai, H. Lu, C. Wu, L. Chen, X. Lin, K. Naoki, G. Chen and J. Chang, *Acta Biomater.*, 2013, **9**, 8004.
50 A. J. Engler, S. Sen, H. L. Sweeney and D. E. Discher, *Cell*, 2006, **126**, 677.
51 Y. Liu, D. Cai, J. Yang, Y. Wang, X. Zhang and S. Yin, *Int. J. Clin. Exp. Med.*, 2014, **7**, 1233.
52 E. A. Vogler, J. C. Graper, H. W. Sugg, L. M. Ler and W. J. Brittain, *J. Biomed. Mater. Res.*, 1995, **29**, 1017.
53 Z. Jia, P. Xiu, M. Li, X. Xu, Y. Shi, Y. Cheng, S. Wei, Y. Zheng, T. Xi and H. Cai, *Biomaterials*, 2016, **75**, 203.
54 Y. Deng, P. Zhou, X. Liu, L. Wang, X. Xiong, Z. Tang, J. Wei and S. Wei, *Colloids Surf., B*, 2015, **136**, 64.
55 Y. K. Jo, B.-H. Choi, C. Zhou, J.-S. Ahn, S. H. Jun and H. J. Cha, *J. Mater. Chem. B*, 2015, **3**, 8102.
56 A. K. Gaharwar, S. M. Mihaila, A. Swami, A. Patel, S. Sant, L. R. Rui, A. P. Marques, M. E. Gomes and A. Khademhosseini, *Adv. Mater.*, 2013, **25**, 3329.
57 G. Kaur, M. T. Valarmathi, J. D. Potts and Q. Wang, *Biomaterials*, 2008, **29**, 4074.
58 Y. Huang, G. Zhou, L. Zheng, H. Liu, X. Niu and Y. Fan, *Nanoscale*, 2012, **4**, 2484.
59 C. Sarmento, Z. B. Luklinska, L. Brown, M. Anseau, P. N. D. Aza, S. D. Aza, F. J. Hughes and I. J. Mckay, *J. Biomed. Mater. Res., Part A*, 2004, **69**, 351.
60 K. L. Wong, C. T. Wong, W. C. Liu, H. B. Pan, M. K. Fong, W. M. Lam, W. L. Cheung, W. M. Tang, K. Y. Chiu, K. D. K. Luk and W. W. Lu, *Biomaterials*, 2009, **30**, 3810.
61 E. Nejati, V. Firouzdor, M. B. Eslaminejad and F. Bagheri, *Mater. Sci. Eng., C*, 2009, **29**, 942.

62 M. Kikuchi, S. Itoh, S. Ichinose, K. Shinomiya and J. Tanaka, *Biomaterials*, 2001, **22**, 1705.
63 L. Fang, L. Yang and P. Gao, *Biomaterials*, 2005, **26**, 347.
64 U. Saran, P. S. Gemini and S. Chatterjee, *Arch. Biochem. Biophys.*, 2014, **561**, 109.
65 S. Pezzatini, L. Morbidelli, R. Solito, E. Paccagnini, E. Boanini, A. Bigi and M. Ziche, *Bone*, 2007, **41**, 523.
66 J. H. Lee, H. L. Jang, K. M. Lee, H. R. Baek, K. Jin, K. S. Hong, J. H. Noh and H. K. Lee, *Acta Biomater.*, 2013, **9**, 6177.
67 M. Rocca, M. Fini, G. Giavaresi, N. N. Aldini and R. Giardino, *Biomaterials*, 2002, **23**, 1017.
68 T. Lu, X. Liu, S. Qian, H. Cao, Y. Qiao, Y. Mei, P. K. Chu and C. Ding, *Biomaterials*, 2014, **35**, 5731.
69 J. Fiedler, C. Brill, W. F. Blum and R. E. Brenner, *Biochem. Biophys. Res. Commun.*, 2006, **345**, 1177.
70 J. L. Crane, L. Xian and X. Cao, *Methods Mol. Biol.*, 2016, **1344**, 287.